

This document is a non-peer reviewed preprint submitted to
EarthArXiv

The manuscript is under review at Journal Of Quaternary Science
under the title:

Holocene tephrochronology of Kerguelen Archipelago, Subantarctic Indian Ocean

It has been co-authored by:

Fabien Arnaud¹, Pierre Sabatier¹, Anouk Leloup¹, Aymerick Servettaz^{1,2}, Bertrand Moine³,
Anne-Lise Develle¹, Stéphane Guédron⁴, Vincent Perrot⁴, Cécile Pignol¹, Jérôme Poulénard¹,
Bernard Fanget¹, Emmanuel Malet¹, Eivind Storen⁵, Jean-Louis Reyss^{1,2}, Nicolas Le Viavan⁶,
Katrien Heirman⁷, Marc De Batist⁷, Elisabeth Michel², Jacques-Louis de Beaulieu⁸, Nathalie
Van der Putten², Jostein Bakke⁵

1) Univ. Grenoble Alpes, Univ. Savoie Mont Blanc, CNRS, EDYTEM, 73000 Chambéry,
France

2) Laboratoire des Sciences du Climat et de l'Environnement (LSCE), CEA, CNRS, 91 Gif-
sur-Yvette

3) Laboratoire Magmas et Volcans, Université Jean Monnet, CNRS, 42023 Saint-Etienne
France

4) Univ. Grenoble Alpes, Univ. Savoie Mont Blanc, CNRS, IRD, IFSTTAR, ISTerre, 38000
Grenoble, France Institut des Sciences de la Terre (ISTerre), Université Grenoble Alpes,
CNRS, Grenoble, France

5) Department of Earth Science and Bjerknes Centre for Climate Research, University of
Bergen, Allégaten 41, 5007 Bergen, Norway

6) Institut Paul-Emile Victor, 29280, Plouzané, France

7) Renard Centre of Marine Geology, Department of Geology, Ghent University, Krijgslaan
281 S8, B-9000 Ghent, Belgium

8) TNO – Geological Survey of the Netherlands, Princetonlaan 6, NL-3584 CB Utrecht,
Netherlands

9) Institut Méditerranéen de Biodiversité et d'Ecologie marine et occidentale (IMBE), Aix-
Marseille Université, CNRS, 13545 Aix en Provence, France

10) Department of Earth Sciences, VU University Amsterdam, De Boelelaan 1085, 1081 HV,
Amsterdam, the Netherlands

43 **Holocene tephrochronology of Kerguelen Archipelago,** 44 **Subantarctic Indian Ocean**

45
46 Fabien Arnaud¹, Pierre Sabatier¹, Anouk Leloup¹, Aymerick Servettaz^{1,2}, Bertrand Moine³,
47 Anne-Lise Develle¹, Stéphane Guédron⁴, Vincent Perrot⁴, Cécile Pignol¹, Jérôme Poulenard¹,
48 Bernard Fanget¹, Emmanuel Malet¹, Eivind Storen⁵, Jean-Louis Reyss^{1,2}, Nicolas Le Viavan⁶,
49 Katrien Heirman⁷, Marc De Batist⁷, Elisabeth Michel², Jacques-Louis de Beaulieu⁸, Nathalie
50 Van der Putten², Jostein Bakke⁵

51
52 1) Univ. Grenoble Alpes, Univ. Savoie Mont Blanc, CNRS, EDYTEM, 73000 Chambéry,
53 France

54 2) Laboratoire des Sciences du Climat et de l'Environnement (LSCE), CEA, CNRS, 91 Gif-
55 sur-Yvette3 : Laboratoire Magmas et Volcans, Université Jean Monnet, CNRS, 42023 Saint-
56 Etienne France

57 4) Univ. Grenoble Alpes, Univ. Savoie Mont Blanc, CNRS, IRD, IFSTTAR, ISTERre, 38000
58 Grenoble, France Institut des Sciences de la Terre (ISTERre), Université Grenoble Alpes,
59 CNRS, Grenoble, France

60 5) Department of Earth Science and Bjerknes Centre for Climate Research, University of
61 Bergen, Allégaten 41, 5007 Bergen, Norway

62 6) Institut Paul-Emile Victor, 29280, Plouzané, France

63 7) Renard Centre of Marine Geology, Department of Geology, Ghent University, Krijgslaan
64 281 S8, B-9000 Ghent, Belgium

65 8) TNO – Geological Survey of the Netherlands, Princetonlaan 6, NL-3584 CB Utrecht,
66 Netherlands

67 9) Institut Méditerranéen de Biodiversité et d'Ecologie marine et occidentale (IMBE), Aix-
68 Marseille Université, CNRS, 13545 Aix en Provence, France

69 10) Department of Earth Sciences, VU University Amsterdam, De Boelelaan 1085, 1081 HV,
70 Amsterdam, the Netherlands

71
72

73 **Abstract**

74 Up to now, no geochemical or geochronological data has been published about Holocene
75 volcanic activity on the Kerguelen Archipelago. Here we present the first continuous
76 Holocene chronology of volcanic eruptions on the archipelago. We compared
77 sedimentological, geochronological and geochemical data from two lake sediment cores taken
78 in two different depocenters of Lake Armor, located ca. 70 km away from the archipelago's
79 main volcanic area. This allowed us to confidently assign the pumice- and ash-rich layers that
80 are interbedded in the lake sediments to distinct volcanic eruptions. Eight main and 3 minor
81 eruptions were thus documented and dated, among which the youngest occurred during the
82 Middle Ages, in AD 1020 +/- 58. The oldest eruption (11,175 +/- 275 cal. BP) is also by far
83 the strongest and deposited, more than 1.2 m of up to 3 cm-large pumices in Lake Armor area.
84 The new tephrostratigraphy presented here may serve as a tool to synchronise
85 paleoenvironmental records from Kerguelen as well as marine records from the Kerguelen rise
86 and beyond. areas.

87

88 **Keywords**

89 **Kerguelen, Lake sediments, Tephrostratigraphy, Subantarctic Indian Ocean,**
90 **Geochemistry**

91

92

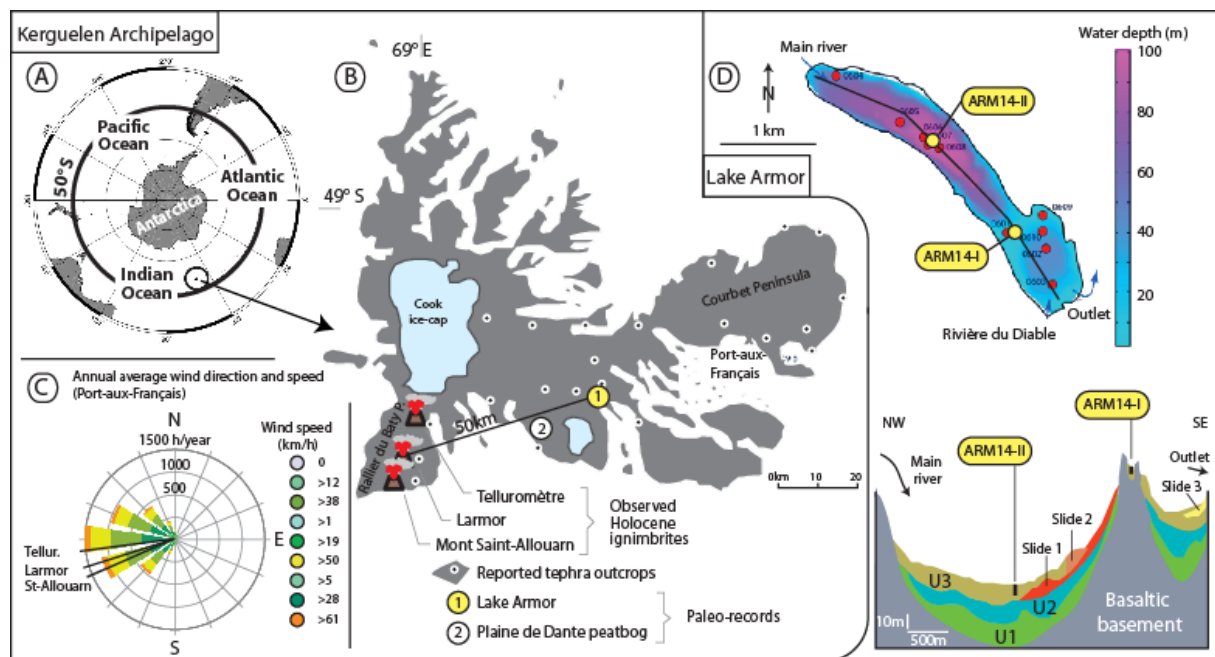
93 **Introduction**

94
95 Kerguelen Archipelago is located in the sub-Antarctic Indian Ocean, several thousands of
96 kilometres away from any continental landmass (Fig. 1). Its location in the vicinity of the
97 current position of the subpolar front and within the southern westerly wind belt, makes it
98 particularly sensitive to global climate change and thus a potential key place for climate
99 reconstruction. Moreover, high-quality, millennial-long scale palaeoecological and
100 paleoclimatological records are still scarce in this part of the world (Oppedal et al., 2018;
101 Saunders et al., 2018; Shulmeister et al., 2004; van der Bilt et al., 2017; Van der Putten et al.,
102 2004, 2008, 2015). This makes Kerguelen a potential key target for paleoenvironmental
103 reconstructions such as changes in oceanic and atmospheric circulation patterns (Sijp and
104 England, 2009). Kerguelen's main island and its dozens of surrounding isles and islets, host a
105 myriad of lakes and peatbogs, holding a great potential for reconstructions of past climate and
106 environment (Arnaud et al., 2016). Lakes in particular are numerous and present a great
107 variety of settings, ranging from small ponds suitable for aDNA ((Ficetola et al., 2018) and
108 biomarker palaeothermometry (Peterse et al., 2014), alpine proglacial lakes that may serve for
109 glacier reconstruction (Dahl et al., 2003; L. T. Oppedal et al., 2018) to fjord-type lakes with
110 large catchments and river systems suitable for paleohydrological reconstructions (Arnaud et
111 al., 2012; Debret et al., 2010; Wessels, 1998). Paleoenvironmental information is particularly
112 robust when such multi-proxy records from different types of lakes are comparable within a
113 precise chronological framework. The restricted vegetation and, in consequence, paucity of
114 terrestrial organic carbon in alpine lake sediments makes the use of radiocarbon dating
115 challenging. It is hence crucial for further studies to establish a common time-scale with
116 ubiquitous tie markers identifiable at least at the archipelago scale. The volcanic nature of the
117 Kerguelen Archipelago, together with indications of recent volcanic activity, makes it
118 possible to use tephrostratigraphy to construct such a chronological framework for correlating
119 different proxy-records (Fontijn et al., 2016; Oppedal et al., 2018).

120
121 Present-day geothermal activity is evidenced by the presence of fumaroles and hot springs on
122 the Rallier Du Baty Peninsula (Fig. 1), in the South-Western part of Kerguelen's main island.
123 Indeed, the most recent evidence of volcanism was found on the Rallier du Baty Peninsula
124 and dated at 26 ± 3 ka BP (Gagnevin et al., 2003). Field observations suggest the existence of
125 more recent volcanic activity as ash and pumice layers of variable thickness were found in
126 peat deposits (Roche-Bellair, 1976; Van der Putten et al., 2015). However, until now no
127 Holocene volcanic deposits have been directly dated and published except for a trachyte of
128 the "Dôme Carva" volcano complex, which was Ar/Ar-dated at about 10 ka (Ethien et al.,
129 2003).

130
131 Here, we present results from the study of two sediment cores from Lake Armor, on
132 Kerguelen's main island (Fig. 1). Both cores contain several well-marked pumice or ash
133 layers. We particularly address the question whether the ash layers are the result of a
134 contemporaneous volcanic eruption or of post-eruptional remobilisation and re-deposition.
135 Every volcanic event deposit is given an age based on radiocarbon dating and the individual
136 layers are geochemically characterised resulting in the first Holocene tephrostratigraphic
137 framework from the Kerguelen Archipelago.

138



139
 140
 141
 142
 143
 144
 145
 146

Fig. 1 A: The Southern Ocean with a circle marking the location of the Archipelago Kerguelen located at 49°S in the sub-Antarctic sector of the Indian Ocean. B: Kerguelen with the main geographical features, the location of the Cook Ice cap and the major volcanos in the south. C: Dominant wind speed and direction, recorded at the French research station at Port-aux-Français. D: Lake sediment core locations in Lake Armor, plotted on a bathymetry map and a simplified seismic profile, based on (Heirman et al., 2012).

2. Setting, material and methods

147
 148
 149
 150
 151
 152
 153
 154
 155
 156
 157
 158
 159

The main island of the Kerguelen Archipelago has a surface area of *ca.* 7215 km². It is the emerged part of the Kerguelen-Gaussberg Oceanic Plateau, which was formed by a series of giant basaltic eruptions *ca.* 40 Ma ago when the SE Indian Ridge (SEIR) overlapped the Kerguelen mantle plume. Since 25 Ma the SEIR migrated to the north but hot spot-type volcanism remained active, due the persistence of the mantle plume (Ethien et al., 2003). Through time, the magmatic activity decreased leading to differentiation processes and a shift toward a more explosive volcanism. Large volcano-plutonic massifs of syenite and trachyte have hence developed during the last 15 Ma in the south-western province of Kerguelen (Gagnevin et al., 2003). Until recently, the youngest volcanic edifice of the island was thought to be the Mont Ross – the highest summit of Kerguelen – which was active between 1 Ma and 130 ka (Weis et al., 1998).

160
 161
 162
 163
 164
 165
 166
 167
 168
 169
 170

Lake Armor is located on Kerguelen's main island, 50 km north-east and downwind from the main volcanic edifices on Rallier du Baty Peninsula (Fig. 1). The lake is located 5m asl, is 4 km long and 500 m wide and separated from the sea by a bedrock sill. Bathymetric and seismic surveys were conducted in 2006 and revealed two sub-basins – 100 and 50 m deep – separated by a 20-m-deep rock-sill (Fig. 1), probably of glacial origin (Heirman et al., 2012). A small isolated depocenter on top of this rock-sill records only the air-borne fraction of allochthonous input, whereas the deeper sub-basins record also river-borne sediments, primarily from the main inlet in the north-western end of the lake. Seismic imaging revealed a post-glacial infilling in which 3 units could be recognised (Fig. 1). NW-facing slopes of the central rock-sill seem instable as they are marked by the presence of two underwater landslides.

171
 172

In 2006, ten short cores were collected from the two main sub-basins, as well as from the small perched depocenter on the sill, using an UWITEC gravity corer. Based on the results of

173 the coring survey and on seismic imagery (Heirman et al., 2012), two sites were selected for
174 retrieving longer cores. These were taken in 2014 using an UWITEC platform and different
175 piston corers. Despite the particularly harsh weather conditions, several cores were collected
176 on each site (Arnaud et al., 2016), giving the opportunity of choosing the optimal cores for
177 tephrochronology and banking material for further studies. From site I (49,4648°S,
178 69,7137°E), a modified Nesje-type corer (Nesje, 1992) designed and built up on the field
179 from parts of an UWITEC Usinger-modified piston corer, was used to take the single run 6.1
180 m long ARM14-I-04 core, which was subsequently split into four sections (S1). From site II
181 (49,45675°S, 69,70193°E), the ARM14-II-03 core was obtained as a composite of a 4 m
182 Nesje-type core (subsequently split into 3 sections), and completed in the same hole by two
183 runs of a 2-m-long UWITEC Niederreiter-type piston corer. Unfortunately, on site II, the
184 sediment below 4 m depth was made of particularly loose non-compacted sand and *ca.* 80 cm
185 were lost at the bottom of each of those runs. The sequence hence reached *ca.* 7.2 m but was
186 fully recovered only down to 4 m, with two additional floating sequences between *ca.* 4 to 5.1
187 m and 6 to 7.2 m (S1).

188 The cores were split into two halves at the EDYTEM laboratory. Each half-section was
189 described in detail and pictures were taken. Lithological description of the sequence allowed
190 the identification of different sedimentary facies.

191
192 X-Ray Fluorescence (XRF) core-scanning was performed for the entire composite sequence
193 with a step size of 5 mm and 0.5 mm for ARM14-I and ARM14-II, respectively, using an
194 Avaatech core-scanner (EDYTEM). X-ray were generated with a Rh anode and geochemical
195 data were obtained with two voltage settings: 10 kV and 1 mA for 20 s for Al, Si, S, K, Ca,
196 Ti, Mn, and Fe and 30 kV and 0.75 mA for 30 s for Cu, Zn, Br, Sr, Rb, Zr, and Pb (Richter et
197 al., 2006). Each individual power spectrum was converted by a deconvolution process into
198 relative components (intensities) expressed in counts per second.

199
200 Sediment core ARM14-I-04 was then subsampled by slicing every 0.5 to 2 cm, depending on
201 the sedimentary facies, in total 591 samples. The dry bulk density (DBD) of each sample was
202 obtained from difference in weight (wet vs dry) after freeze-drying. The 591 sampled volumes
203 were between 1 and 5.5 cm³ and densities vary between 0.17 to 1.18 g.cm⁻³. Each sediment
204 slice was then ground (< 63 μm) using agate mortars for further chemical analysis. For each
205 sample, total Hg concentration (THg) was determined by atomic absorption
206 spectrophotometry following dry mineralization and gold amalgamation using an automatic
207 mercury analyzer [Altec, model AMA 254 (Guédron et al. 2009)]. Quality control for THg
208 analysis was performed by periodic measurements of blanks (n=73), certified reference
209 materials [CRMs: IAEA-158 (n=26), NRCC MESS-3 (n=40) and BCR-679 (n=5)], and
210 sample replicates (n=48). The measurement error was 6.2 % on average and always below 10
211 %. THg was quantified introducing 100 to 200 mg of dry weight sample, leading to a mass of
212 Hg between 0.6 to 40 ng, while the detection limit was 55 pg of Hg (3SD of blank) and the
213 quantification limit was 185 pg of Hg (10SD of blank). The 3 CRMs showed excellent
214 recoveries with values of 128.1 ± 6.2 ng g⁻¹ (certified value = 132 ± 14 ng g⁻¹) for IAEA-158,
215 92.9 ± 2.3 ng g⁻¹ (certified value = 91 ± 9 ng g⁻¹) for MESS-3, and 6.9 ± 0.6 ng g⁻¹ (certified
216 value = 6.3 ± 1.4 ng g⁻¹) for BCR-679. Measurement error on sample replicates ranged from
217 0.03 to 5.38 %.

218
219 Eleven samples of glass shards and pumice layers were selected for major element analysis of
220 glass with an electron microprobe CAMECA© SX100 (Magmas & Volcanoes Laboratory in
221 Clermont-Ferrand, France). Tephra samples were embedded in epoxy resin, polished and
222 carbon metallized. Specific setting for glass analysis was used (low current intensity 5 nA, 15

223 keV, long count for Na and K- 60 s, and background after peak measurement). Only 8 over
224 the 11 samples yielded statically acceptable results.

225
226 Laser Ablation coupled with an ICP-MS was used to analyse the trace and rare earth elements
227 (REE) composition of three samples of glass shards and pumices (also at Magmas &
228 Volcanoes Laboratory in Clermont-Ferrand). The equipment used was an excimer laser
229 system 193 nm Resonetics M-50E, completely computer-controlled and equipped with a laser
230 ATL ultra short pulse duration (< 4 ns), coupled to an ICP-MS spectrometer Agilent 7500
231 with an optical "cs" high sensitivity and a strengthened pump interface. Reproducibility and
232 accuracy of the analyses was estimated through repeated analyses of BCR-2g standard at the
233 beginning and at the end of each run. Data reduction was carried out with the software
234 package GLITTER (Macquarie Research Ltd, 2001 ; van Achterbergh et al., 2001). For each
235 analysis, the time-resolved signal for each element was monitored to discard perturbations
236 related to inclusions, fractures or mixing.

237
238 The upper 10 cm of core ARM14-II were sampled every 5 mm for short-lived radionuclide
239 measurements, using high-efficiency, very low-background, well-type Ge detectors at the
240 Modane Underground Laboratory (LSM) (Reyss et al., 1995). Counting times of 24 to 48
241 hours were required to reach a statistical error of less than 10 % for excess ^{210}Pb in the
242 deepest samples and for the ^{137}Cs peak. In each sample, the ^{210}Pb excess activities ($^{210}\text{Pb}_{\text{ex}}$)
243 were calculated by subtracting the ^{226}Ra -supported activity from the total ^{210}Pb activity.

244
245 Twelve and 14 samples of plant macro-fossils were taken from ARM14-I and ARM14-II,
246 respectively, for AMS radiocarbon dating. Radiocarbon content was measured at the
247 Laboratoire de Mesure 14C (LMC14) ARTEMIS at the CEA (Atomic Energy Commission)
248 institute at Saclay (samples referenced with the prefix Sac in Tab 1) and at the Poznan
249 Radiocarbon Laboratory (samples referenced with the prefix Poz in Tab 1). Remains of
250 terrestrial plants were preferred, except in core ARM14-I, which did not contain any, and for
251 which radiocarbon dating was done on aquatic plant fragments. However, as there is no
252 carbonate in the catchment, we do not expect any significant reservoir effect. Radiocarbon
253 ages were calibrated using the SHcal04 calibration curve (McCormac et al., 2004). Then, we
254 used "clam" (version 3.0.2), the R-based (R Development Core Team, 2011) algorithm
255 developed by Blaauw (2010), to generate an age/depth model.

256
257

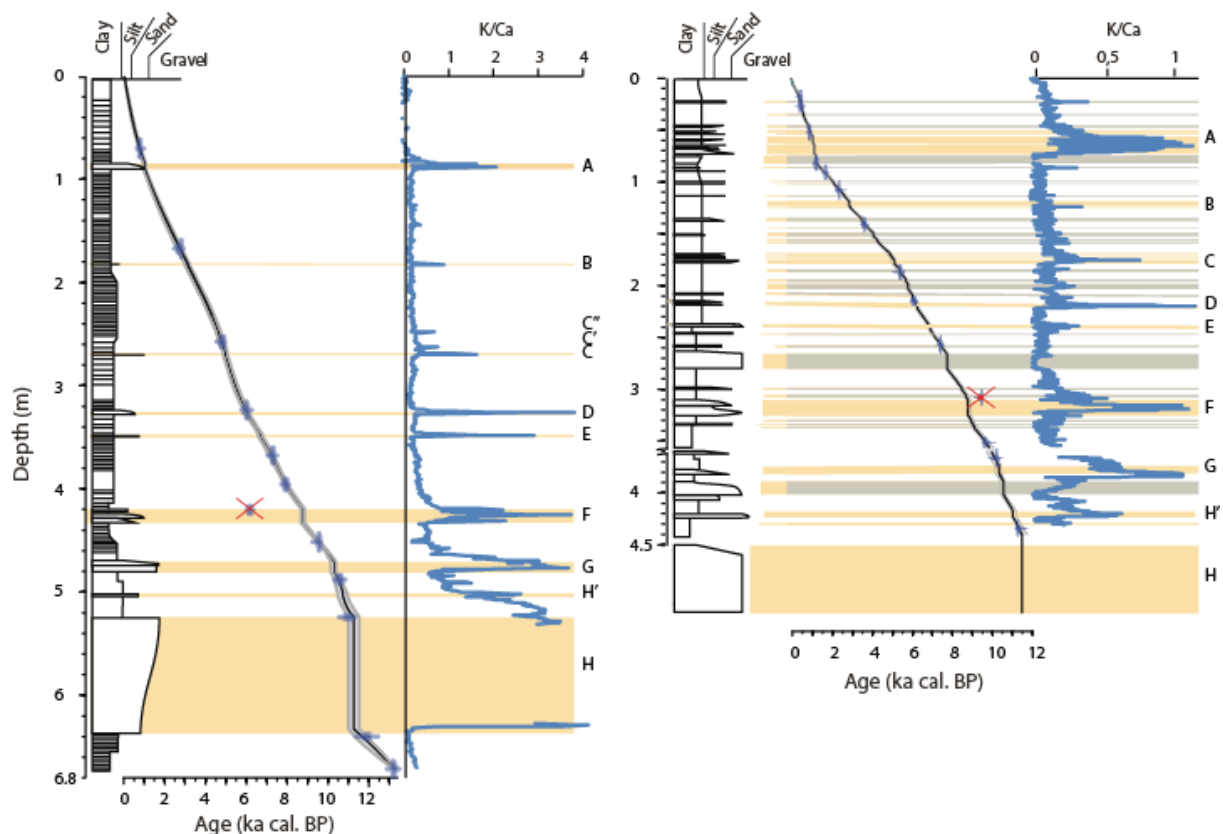
258 **3. Results and discussion**

259 260 **3.1. Core description and lithology**

261
262 On site ARM14-I, the sediment consists of a brownish fine mud (Fig. 2), rich in plant
263 remains. This is consistent with field observations of large bryophytes living at the bottom of
264 the lake in this shallow sub-basin (20 m). The continuous sedimentation is interrupted by nine
265 mineral-rich layers, with grainsize ranges from fine silt up to >1 cm gravels. Seven of those
266 layers contain white mm- to cm-large pumices. The most outstanding feature is a thick
267 pumice layer located between 5.25 and 6.35 m below the lake floor. This layer have an
268 inverse grading, which is typical for sub-aquatic pumice deposits, as larger pumices float
269 better than smaller ones and thus sink later following the pumice rain (Ikehara, 2015). Visible
270 ash and pumice identified in core ARM14-I were labelled from top to bottom, from A to H.
271 The pumice layer identified at 5 m was labelled H' as it is not clear, according to the

272 stratigraphic description, whether it is an individual event or a sub-event following the main
273 pumice-deposit event (H).
274

275 Site ARM14-II presents the same facies of continuous sedimentation as ARM14-I, but with a
276 more complex stratigraphy in terms of interbedded deposits. Indeed, in addition to ash and/or
277 pumice layers, several mm- to cm-thick mineral-enriched fine silt layers are also present.
278 Moreover, the number of pumice layers is higher here than in ARM14-I. Because of this
279 complexity it is not straightforward to correlate both sequences. However, two outstanding
280 features can be recognized: i) the uppermost pumice and ash sequence (85-90 cm in ARM14-
281 I; 50-65 cm in ARM14-II), and ii) the lowermost thick and coarse pumice layer. For both
282 features, deposits in ARM14-II appear to be more complex than those in ARM14-I. The
283 higher number of pumice layers in ARM14-II suggests that this site is submitted to sediment
284 remobilisation and re-deposition. Considering the shape of the lake and the available seismic
285 data (Fig. 1), this sediment reworking may originate from the northern flank of the central
286 rock-sill – at the top of which ARM14-I was taken – or from the main river delta (Heirman et
287 al., 2012).
288



289
290 Fig. 2: Stratigraphic description, age model and K/Ca ratio for the ARM14-I (left) and ARM14-II (right) cores.
291 Rejected ^{14}C ages are identified by a red cross, see table 1. Letters on the right part of each panel are identified
292 tephra layers. Yellow stripe highlight layers interpreted as tephra deposits. Grey stripes highlight ARM14-II
293 layers interpreted as *a posteriori* volcanic material reworking.
294

295 3.2 Chronology

296
297 A logarithmic plot of ($^{210}\text{Pb}_{\text{ex}}$) activities for ARM14-II (SI2) shows a linearly decreasing
298 trend. According to the constant flux, constant sedimentation rate (CFCS) model (Goldberg,
299 1963), using the 'serac' R package (Bruel and Sabatier, 2020), the mean accumulation rate is
300 $1.068 \pm 0.070 \text{ mm.y}^{-1}$ for the upper 10 cm (SI). The profile of ^{137}Cs (SI2) displays an increase

301 at a depth of 6 cm and a peak between 4 and 5.5 cm. According to other studies from the
302 Southern Hemisphere, the lower peak corresponds to the first appearance of ^{137}Cs at AD
303 1955, and the upper, peak to AD 1965 (Arnaud et al., 2006; Ficetola et al., 2018). This
304 temporal correlation is supported by the ^{241}Am peak at the same depth, which was a result of
305 the decay of ^{241}Pu in fallout from atmospheric nuclear weapons tests (Appleby, 1991). The
306 good agreement between the ages derived from the $^{210}\text{Pb}_{\text{ex}}$ -CFCS model, and the artificial
307 radionuclide peaks provide a well-constrained, continuous age-depth relationship for the
308 upper 60 cm of ARM14-II (SI2).

309
310 Vegetal macro-remains were collected for radiocarbon dating from core ARM14-I (12
311 samples) and ARM14-II (14 samples) (Table 1). Two radiocarbon ages were excluded, one is
312 too old compared to the others (core ARM14-II), probably due to re-mobilisation and re-
313 deposition of macro-remains stored in the lake catchment area, and the other too young in
314 ARM14-I, possibly caused by contamination during sampling (Fig. 2). Events
315 (=instantaneous sedimentation) such as tephra and reworked layers were removed in both
316 sequences prior to age-depth modelling. The calculated age-depth relationship was done
317 using a smooth spline function using the R-based algorithm “clam” (version 2.2; Blaauw,
318 2010) with integration of the short-lived radionuclide-derived ages for ARM14-II. This age-
319 depth model was used to date all instantaneous deposits. The vertical bars represent the age of
320 each event thicker than 5 mm with uncertainties (2σ) resulting from the ^{14}C ages (Fig. 2). The
321 first 670 cm of ARM14-I and the first 470 cm of ARM14-II covered the last 13 and 11,5 kyr
322 cal BP, respectively. The event-free sedimentation rate for ARM14-II ranges between 0.16
323 and 0.83 mm yr^{-1} , with a mean of 0.3 mm.yr^{-1} . For ARM14-I the mean event-free
324 sedimentation rate is 0.43 mm.yr^{-1} , ranging between 0.14 and 0.83 mm yr^{-1} , below 45 cm
325 sediment depth, and increases to 1,67 mm.yr^{-1} for the upper 45 cm, probably in relation to the
326 higher water content of this organic rich sediment.
327

Cores	Samples	MCD (m)	Age BP	Age range cal BP
ARM14I	Poz-77362	0,7	800±40	575-744
ARM14I	SacA42461	1,7	2605±30	2497-2757
ARM14I	SacA42462	2,61	4225±30	4584-4838
ARM14I	Poz-77363	3,27	5200±3,15	5752-5995
ARM14I	SacA42463	3,71	6320±35	7028-7294
ARM14I	Poz-77285	4	7030±40	7709-7932
ARM14I	SacA42464	4,25	5335±35	5943-6188
ARM14I	SacA42465	4,56	8485±45	9320-9535
ARM14I	SacA42466	4,93	9345±45	10297-10653
ARM14I	Poz-77286	5,32	9580±60	10663-11125
ARM14I	poz- 73369	6,57	10200±50	11503-12029
ARM14I	SacA42467	6,89	11320±50	13056-13256
ARM14II	SacA-12202	0,18	360±30	310-467
ARM14II	SacA-9751	0,263	425±60	317-515
ARM14II	Poz-69603	0,52	970±30	772-918
ARM14II	Poz-69604	0,81	1295±30	1075-1268
ARM14II	Poz-89883	0,91	1775±30	1571-1713
ARM14II	Poz-69605	1,08	2355±35	2181-2455
ARM14II	Poz-69606	1,41	3395±35	3479-3691
ARM14II	Poz-69607	1,87	4680±40	5146-5575

ARM14II	Poz-89884	2,14	5340±40	5941-6203
ARM14II	Poz-89885	2,56	6540±40	7311-7496
ARM14II	Poz-89887	3,06	8460±50	9304-9528
ARM14II	Poz-89888	3,51	8720±50	9535-9885
ARM14II	Poz-89889	3,65	9090±50	9941-10373
ARM14II	Poz-89891	4,35	9920±50	11194-11596

Table 1. ¹⁴C ages for ARM14I and ARM14II master cores, in bold ages removed for chronology modelling.

328
329

330
331

3.3. Identification and age of volcanic-related layers

332
333
334
335
336
337
338
339
340
341

In order to identify more precisely the occurrence of volcanically triggered deposits, both cores were logged on a XRF core scanner. When compared to surrounding basaltic bedrock, Kerguelen most recent volcanic emissions are enriched in potassium (K) relative to calcium (Ca) (Gagnevin et al., 2003), we thus hypothesised that the ratio K/Ca could be a good proxy for the presence of volcanic-triggered layers, as no carbonates are present in the sediment. The XRF-based chemical stratigraphy of ARM14-I confirms this hypothesis, i.e. each tephra layer identified by visual description shows an increase in K/Ca (Figure 2 and 3). Core logging hence led to identify two cryptotephra, which seem to have followed within some decades to centuries the eruption C and further referred as tephra deposits C' and C''.

342
343
344
345
346
347
348
349
350
351

We further used high-resolution mercury (Hg) measurements as an additional conformation for the presence of these tephra deposits (Daga et al., 2016; Guédron et al., 2019; Ribeiro Guevara et al., 2010). During volcanic eruptions, the rapid deposition of massive inorganic volcanoclasts (tephras) results in abrupt drops in the Hg concentration profile (down to 0.9 ng g⁻¹) diluting the uninterrupted organic-rich sediment deposits (average THg = 23.7 ± 6.7 ng g⁻¹) that have accumulated Hg from the atmosphere. For all potential volcanically triggered event deposits (even the cryptotephra C' and C''), the Hg profile depicts a pattern that is mirrored compared to the K/Ca profile, and presents 2 to 20 fold decreases in Hg concentration compared to the baseline value of uninterrupted sedimentation (Fig. 4A).

352
353
354
355
356
357
358
359
360
361
362
363
364
365
366

We further used high-resolution mercury (Hg) measurements as an additional conformation for the presence of these tephra deposits. While volcanoes are a major natural Hg source in the environment through the atmospheric emission of gaseous elemental Hg (Bagnato et al., 2011), during volcanic eruptions the rapid deposition of massive inorganic volcanoclasts (tephras) results in abrupt drops in the local Hg concentration profiles (Daga et al., 2016; Guédron et al., 2019; Ribeiro Guevara et al., 2010). This is the case here with the lowest Hg content measured in tephra (down to 0.9 ng g⁻¹), as compared to the uninterrupted organic-rich sediment deposits (average THg = 23.7 ± 6.7 ng g⁻¹) that have accumulated Hg from the atmosphere. For all potential volcanically triggered event deposits (even the cryptotephra C' and C''), the Hg profile depicts a pattern that is mirrored compared to the K/Ca profile, and presents 2 to 20 fold decreases in Hg concentration compared to the baseline value of uninterrupted sedimentation (Fig. 4A). In a future work, high resolution pre- and post-depositional Hg variations will be discussed thoroughly with geochemical proxies and meteorological factors throughout the entire ARM14-I sediment core.

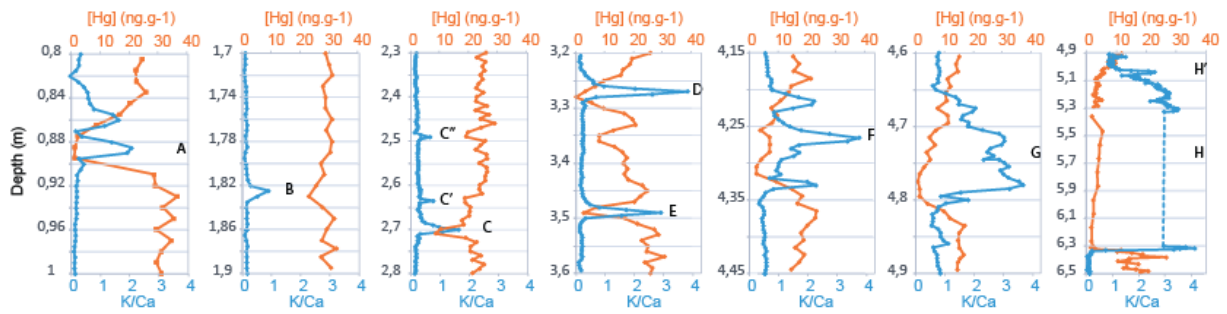


Figure 3. Detection of macro- and cryptotephra deposits using both K/Ca and [Hg] proxies

367
 368
 369
 370
 371
 372
 373
 374
 375
 376
 377
 378

The chemical stratigraphy combined with independent age-depth models of both cores allowed to determine the event layers that were deposited contemporaneously at both sites (Figures 2 and 3). For this, we applied the following double criterion: i) the presence of a peak in K/Ca, and ii) temporal correlation of similar deposits in both cores. Using this approach, it was possible to correlate all main event deposits in ARM14-I and ARM14-II (Fig. 4). However, in order to assess the intensity of triggering eruptions we used core ARM14-I only because it is solely submitted to direct atmospheric fallout, whereas site II receives input from both direct fallout and river-borne reworked material. Figure 4 shows the thickness of tephra layers and their average grain size.

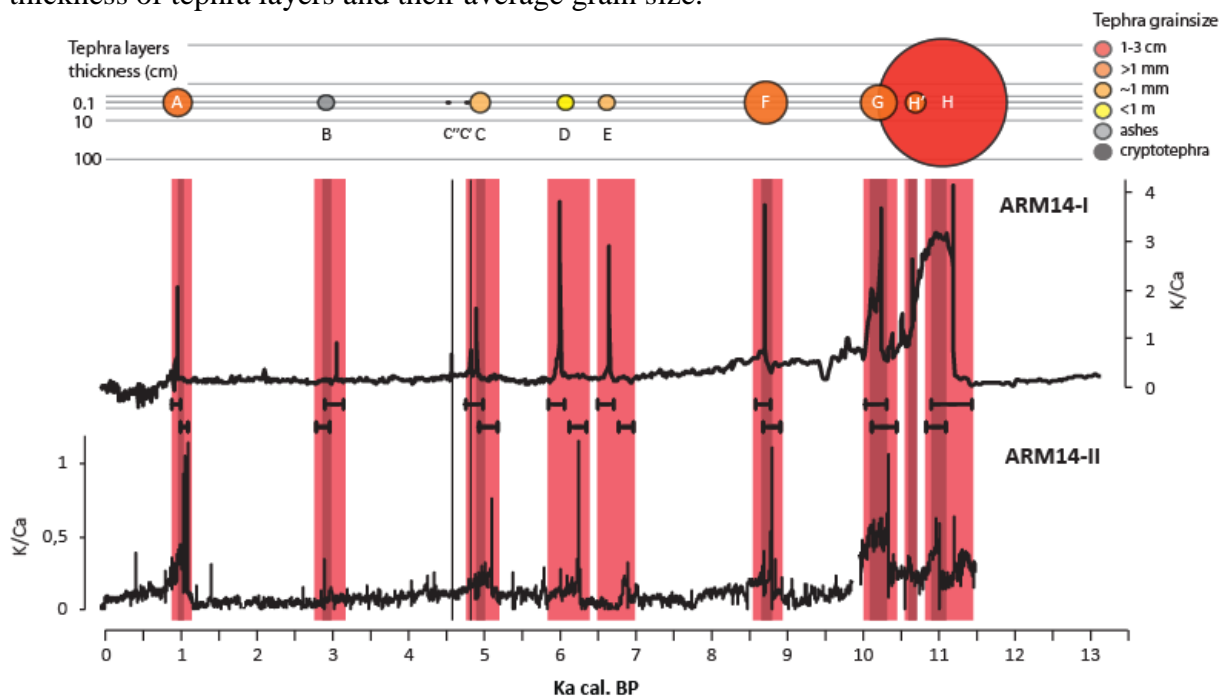


Fig. 4: Synoptic representation of Kerguelen tephrostratigraphy. The upper panel shows the thickness and grain size of tephra in core ARM14-I. The lower panel displays K/Ca ratios in ARM14-I and ARM14-II in relation to age. Light red bands correspond to age uncertainties and dark red bands represent shared age interval in both cores of each tephra layer.

379
 380
 381
 382
 383
 384
 385
 386
 387
 388
 389
 390
 391

This analysis leads to the identification of 8 main volcanic eruption events over the last 13,000 years, labelled A to H, from the youngest to the oldest, and 3 smaller events, following shortly after a larger one, labelled C' and C'' (following eruption C) and H' (following eruption H). We note a high recurrence of events in the early Holocene: i.e. ca. 1 event per millennium. These early Holocene events appear also to have been stronger than subsequent events, as they all produced tephra layers of 1 to 10 cm in thickness. Only four weaker events (all in the thickness range of 0.1 to 1 cm, or below) occurred between 1,000 (layer A) and

392 8,500 ka cal. BP (layer F), i.e. a mean recurrence interval of 1 event every 2 millennia. The
393 very last eruption occurred only ca. 1,000 years ago and brought a pumice layer thicker and
394 coarser than any of the eruptions since 8,500 ka cal. BP.

395 X-Ray Fluorescence (XRF) core-scanning was performed for the entire composite sequence
396 with a step size of 5 mm and 0.5 mm for ARM14-I and ARM14-II, respectively, using an
397 Avaatech core-scanner (EDYTEM). X-ray were generated with a Rh anode and The
398 geochemical data were obtained with two tubetwo voltage settings: 10 kV and 1 mA for 20 s
399 for Al, Si, S, K, Ca, Ti, Mn, and Fe and 30 kV and 0.75 mA for 30 s for Cu, Zn, Br, Sr, Rb,
400 Zr, and Pb (Richter et al., 2006). Each individual power spectrum was converted by a
401 deconvolution process into relative components (intensities) expressed in counts per second.

402 The oldest event has also been the one yielding the most important amount of pumices to
403 Lake Armor. With more than 1m of deposit without any focusing factor at site I and a
404 maximum pumice size of several centimetres, it is probable that this event that occurred 70km
405 away from our study site has been of extreme explosiveness.
406

Tephra #		A	B	C''	C'	C	D	E	F	G	H'	H
Depth (cm)	Top	85	178	249	263	268,5	328	348	420	472	510	524,5
	Bottom	90,5	179	249	263	270,5	328	349,5	433,5	481	513	633
Age (cal. BP)	min95%	872	2803	4423	4675	4766	5875	6510	8610	10054	10497	10927
	best	944	2950	4559	4805	4894	6003	6649	8705	10246	10737	11191
	max95%	998	3045	4680	4913	4999	6087	6726	8796	10333	10995	11457
Thickness (cm)	6	2	<0,1	<0,1	3	1	1,5	13,5	9	3	109	
Visual description	> 1 mm pumices	ash layer	cryptotephra	cryptotephra	~1 mm pumices	< 1mm pumices	~1 mm pumices	> 1 mm pumices	> 1 mm pumices	> 1 mm pumices	1-3 cm pumices	
Number of microprobe data		3	0	0	4	8	7	0	7	8	7	5
SiO ₂	%	64,78			64,69	62,92	64,16		64,87	64,33	65,28	64,21
	+/- 1 sigma	0,47			0,65	1,10	0,55		1,01	1,21	0,87	0,79
TiO ₂	%	0,36			0,40	0,53	0,46		0,42	0,34	0,31	0,33
	+/- 1 sigma	0,04			0,06	0,09	0,02		0,07	0,03	0,07	0,03
Al ₂ O ₃	%	15,58			15,68	16,50	16,53		15,84	15,76	14,82	15,75
	+/- 1 sigma	0,17			0,75	0,74	0,13		0,89	0,46	1,16	0,34
MgO	%	0,09			0,07	0,26	0,26		0,13	0,10	0,14	0,21
	+/- 1 sigma	0,02			0,09	0,09	0,04		0,07	0,04	0,10	0,02
FeO	%	5,04			4,61	4,94	4,38		4,79	4,45	4,79	4,52
	+/- 1 sigma	0,29			0,22	0,45	0,28		0,16	0,12	0,38	0,14
MnO	%	0,17			0,24	0,22	0,16		0,18	0,18	0,18	0,24
	+/- 1 sigma	0,08			0,13	0,08	0,09		0,12	0,10	0,06	0,06
CaO	%	0,88			0,84	1,18	1,07		0,99	0,88	0,75	0,88
	+/- 1 sigma	0,06			0,19	0,14	0,02		0,24	0,09	0,22	0,05
Na ₂ O	%	6,85			6,80	6,24	6,19		6,45	6,51	6,52	6,24
	+/- 1 sigma	0,05			0,32	0,39	0,19		0,33	0,18	0,34	0,22
K ₂ O	%	5,25			5,44	5,81	5,93		5,39	5,31	5,15	5,55
	+/- 1 sigma	0,13			0,36	0,38	0,12		0,33	0,18	0,48	0,04

Tab. 2. List of trachytic volcanic deposits identified in core ARM14-I, with their depth in the core, estimated age, thickness, visual description and when available, major element concentrations

3.4 Geochemical characterisation and origin of tephra deposits

414 The geochemical characteristics of the tephra together with the very close proximity of
415 trachytes that were described on Rallier du Baty Peninsula confirms their trachytic origin
416 (Fig. 5A). The hypothesis of a local origin is hence strongly supported. Moreover, the closest
417 landmasses up-wind are the Crozet Archipelago (1300 km) and the Prince Edward Islands
418 (2300 km), which did not produce trachytic volcanism.

420 Major element analyses indicate that tephra can be attributed to an alkaline silica-saturated
421 magmatic series. The concentrations of Na₂O + K₂O and SiO₂ display a very low variability
422 (Fig 5B). This can be explained, despite an intense fractional crystallization process, by the
423 fact that the trachytic magma has reached the azeotrope of the alkali feldspars and therefore

424 the magmatic liquid has the same composition as anorthose, which crystallizes. Only a change
 425 in water activity can allow a change in the major element composition of melts to rhyolitic
 426 magmas. Contrarily, the rare earth element (REE) composition displays a significant
 427 variability, illustrating the fractional crystallization process over time in a magma chamber
 428 emptied by successive episodes (Fig. 5A). This is well illustrated by a progressive decrease of
 429 compatible elements, such as Eu, and an increase of highly incompatible elements as other
 430 REE over time.

431
 432 It is not clear yet if all tephra come from the same volcano and/or the same magma chamber.
 433 Indeed, if REEs show an increasing concentration during successive eruptions, this is not the
 434 case for major and minor elements (CaO, TiO₂) of tephra H, which show distinct
 435 compositions. It is quite possible, given the age data already obtained on Rallier du Baty
 436 Peninsula (Ethien et al., 2003), that the most recent tephra come from the eruptive centre of
 437 Mont Saint-Allouarn in the south of the peninsula and that the tephra H comes from another
 438 eruptive centre further north of the peninsula.
 439

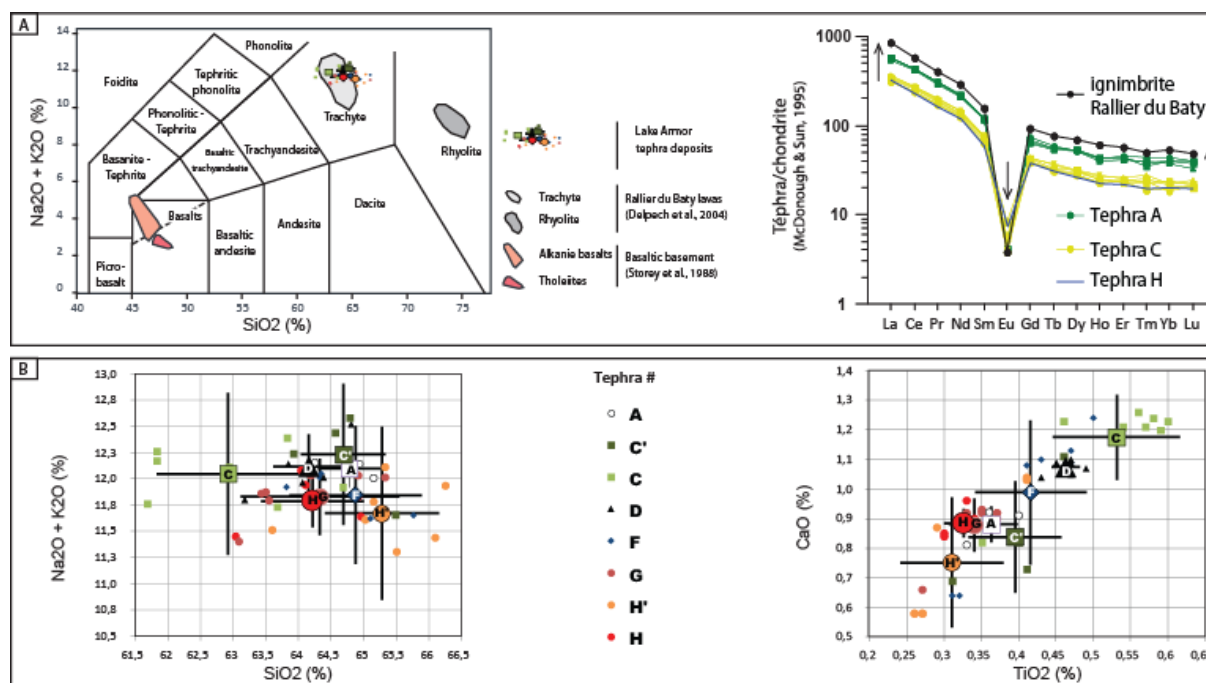


Fig. 5. Geochemical characterisation of Kerguelen tephra deposits.

440
 441
 442
 443
 444

Conclusion

445 Our first attempt to build a tephrostratigraphic framework for the Kerguelen Archipelago
 446 resulted in a list of 8 main Holocene volcanic events (A, B, C, D, E, F, G and H), to which 3
 447 minor events may be added (C', C'' and H'). Their geochemical composition, as well as their
 448 computed ages are given in Table II. Ongoing studies on cores from several lakes in the
 449 Kerguelen Archipelago will benefit from this first framework, and will allow to synchronise
 450 the records.

451
 452 Whereas no evidence of Holocene volcanic activity had previously been published, our results
 453 show eight main Holocene volcanic events (A, B, C, D, E, F, G and H) as well as three minor
 454 events (C', C'' and H') giving a mean return period of one event per millennium. The last
 455 eruption occurred ca. 1,000 years ago and was significantly stronger than any of the eruptions
 456 during the last 8,500 ka cal. BP. The biggest eruption is also the oldest and occurred close to

457 the onset of the Holocene (11 ka cal. BP). The geochemical composition of the deposits
458 points to a common origin local source at the Rallier-du-Baty Peninsula SW Kerguelen.
459 Ongoing studies on cores from several lakes in the Kerguelen Archipelago will benefit from
460 this first framework, and will allow robust synchronising of new records.

461

462 **Acknowledgements**

463 We are warmly grateful to IPEV, the French Polar Institute, for providing necessary logistical
464 support for field expeditions (programmes 448-PEISACG, 444-DyLIOKer, 1094-PALAS).
465 Roland Pagni and Dries Boone are warmly thanked for their help on the field. The authors
466 thank the French CNRS-INSU national coring facility and in particular project ANR-11-
467 EQPX-0009-CLIMCOR, for providing coring facilities. Radiocarbon dates referred as SacA
468 were performed at LMC14 facility in Saclay, in the framework of the national programme
469 ARTEMIS. The authors express their grateful thanks to the LMC14 team, in particular to
470 Jean-Pascal Dumoulin, as well as to Tomas Goslar from Poznan Radioacarbon Laboratory for
471 constant help in the management of ¹⁴C samples and results. XRF core scanning was
472 performed thanks at EDYTEM lab as part of the CEMBRO regional analytical facility. The
473 authors thank the Laboratoire Souterrain de Modane (LSM) facilities for the gamma
474 spectrometry measurements and Environnement, Dynamique et Territoires de Montagne
475 (EDYTEM) for the core scanner X-ray fluorescence analyses. This is Laboratory of
476 Excellence ClerVolc contribution n°XXX. The Norwegian contribution was funded by the
477 Norwegian Research Council under the project Shifting Climate States of the Polar Regions
478 (SHIFTS) (project number; 210004).

479

480

481 Appleby, P.G., 1991. 241Am dating of lake sediments. *Hydrobiologia* 214, 35–42.

482 Arnaud, F., Fanget, B., Malet, E., Poulénard, J., Eivind, S., Leloup, A., Jostein, B., Sabatier,
483 P., 2016. Extensive lake sediment coring survey on Sub-Antarctic Indian Ocean
484 Kerguelen Archipelago (French Austral and Antarctic Lands), in: *Geophysical*
485 *Research Abstracts*. Presented at the EGU General Assembly 2016, EGU, Vienne,
486 Autriche, p. 12876.

487 Arnaud, F., Magand, O., Chapron, E., Bertrand, S., Boës, X., Charlet, F., Mélières, M.-A.,
488 2006. Radionuclide dating (210Pb, 137Cs, 241Am) of recent lake sediments in a
489 highly active geodynamic setting (Lakes Puyehue and Icalma—Chilean Lake District).
490 *Sci. Total Environ.* 366, 837–850. <https://doi.org/10.1016/j.scitotenv.2005.08.013>

491 Arnaud, F., Révillon, S., Debret, M., Revel, M., Chapron, E., Jacob, J., Giguet-Covex, C.,
492 Poulénard, J., Magny, M., 2012. Lake Bourget regional erosion patterns reconstruction
493 reveals Holocene NW European Alps soil evolution and paleohydrology. *Quat. Sci.*
494 *Rev.* 51, 81–92. <https://doi.org/10.1016/j.quascirev.2012.07.025>

495 Bagnato, E., Aiuppa, A., Parello, F., Allard, P., Shinohara, H., Liuzzo, M., Giudice, G., 2011.
496 New clues on the contribution of Earth’s volcanism to the global mercury cycle. *Bull.*
497 *Volcanol.* 73, 497–510. <https://doi.org/10.1007/s00445-010-0419-y>

498 Blaauw, M., 2010. Methods and code for ‘classical’ age-modelling of radiocarbon sequences.
499 *Quat. Geochronol.* 5, 512–518.

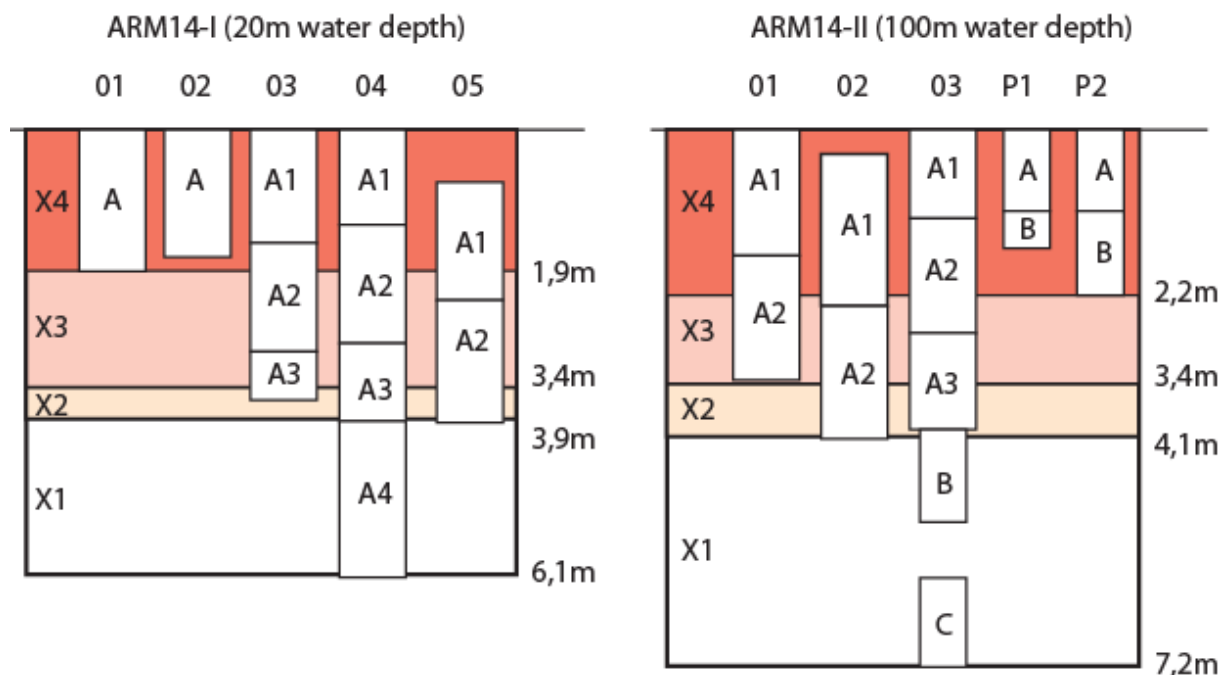
500 Bruel, R., Sabatier, P., 2020. serac: a R package for Shortlived Radionuclide Chronology of
501 recent sediment cores (preprint). *EarthArXiv*. <https://doi.org/10.31223/osf.io/f4yma>

502 Daga, R., Ribeiro Guevara, S., Pavlin, M., Rizzo, A., Lojen, S., Vreča, P., Horvat, M.,
503 Arribére, M., 2016. Historical records of mercury in southern latitudes over
504 1600years: Lake Futalaufquen, Northern Patagonia. *Sci. Total Environ.* 553, 541–550.
505 <https://doi.org/10.1016/j.scitotenv.2016.02.114>

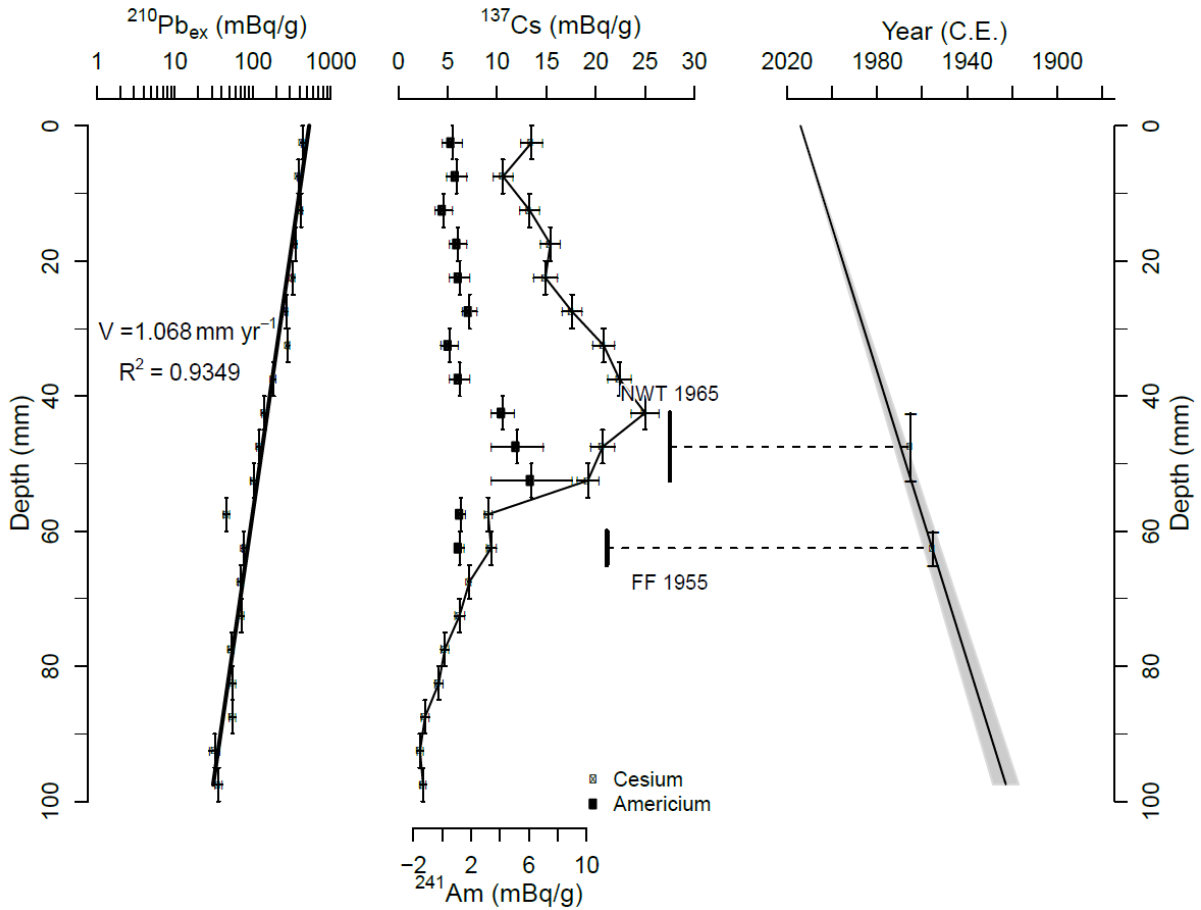
- 506 Dahl, S.O., Bakke, J., Lie, Ø., Nesje, A., 2003. Reconstruction of former glacier equilibrium-
507 line altitudes based on proglacial sites: an evaluation of approaches and selection of
508 sites. *Quat. Sci. Rev.* 22, 275–287. [https://doi.org/10.1016/S0277-3791\(02\)00135-X](https://doi.org/10.1016/S0277-3791(02)00135-X)
- 509 Debret, M., Chapron, E., Desmet, M., Rolland-Revel, M., Magand, O., Trentesaux, A., Bout-
510 Roumazeille, V., Nomade, J., Arnaud, F., 2010. North western Alps Holocene
511 paleohydrology recorded by flooding activity in Lake Le Bourget, France. *Quat. Sci.*
512 *Rev.* 29, 2185–2200. <https://doi.org/10.1016/j.quascirev.2010.05.016>
- 513 Ethien, R., Feraud, G., Gerbe, M.C., Cottin, J.Y., O'Reilly, S.Y., Giret, A., 2003.
514 Geochemistry and Ar/Ar dating of upper pleistocene volcanic rocks from Kerguelen
515 islands (Indian Ocean). Presented at the EGS - AGU - EUG Joint Assembly, p. 6432.
- 516 Ficetola, G.F., Poulenard, J., Sabatier, P., Messenger, E., Gielly, L., Leloup, A., Etienne, D.,
517 Bakke, J., Malet, E., Fanget, B., Støren, E., Reyss, J.-L., Taberlet, P., Arnaud, F.,
518 2018. DNA from lake sediments reveals long-term ecosystem changes after a
519 biological invasion. *Sci. Adv.* 4, eaar4292. <https://doi.org/10.1126/sciadv.aar4292>
- 520 Fontijn, K., Rawson, H., Van Daele, M., Moernaut, J., Abarzúa, A.M., Heirman, K., Bertrand,
521 S., Pyle, D.M., Mather, T.A., De Batist, M., Naranjo, J.-A., Moreno, H., 2016.
522 Synchronisation of sedimentary records using tephra: A postglacial
523 tephrochronological model for the Chilean Lake District. *Quat. Sci. Rev.* 137, 234–
524 254. <https://doi.org/10.1016/j.quascirev.2016.02.015>
- 525 Gagnevin, D., Ethien, R., Bonin, B., Moine, B., Féraud, G., Gerbe, M.C., Cottin, J.Y.,
526 Michon, G., Tourpin, S., Mamias, G., Perrache, C., Giret, A., 2003. Open-system
527 processes in the genesis of silica-oversaturated alkaline rocks of the Rallier-du-Baty
528 Peninsula, Kerguelen Archipelago (Indian Ocean). *J. Volcanol. Geotherm. Res.* 123,
529 267–300. [https://doi.org/10.1016/S0377-0273\(02\)00509-7](https://doi.org/10.1016/S0377-0273(02)00509-7)
- 530 Goldberg, E.D., 1963. Geochronology with 210Pb, in: *Radioactive Dating*. pp. 121–131.
- 531 Guédron, S., Tolu, J., Brisset, E., Sabatier, P., Perrot, V., Bouchet, S., Develle, A.L., Bindler,
532 R., Cossa, D., Fritz, S.C., Baker, P.A., 2019. Late Holocene volcanic and
533 anthropogenic mercury deposition in the western Central Andes (Lake Chungará,
534 Chile). *Sci. Total Environ.* 662, 903–914.
535 <https://doi.org/10.1016/j.scitotenv.2019.01.294>
- 536 Heirman, K., De Batist, M., Arnaud, F., De Beaulieu, J.-L., 2012. Seismic stratigraphy of the
537 late Quaternary sedimentary infill of Lac d'Armor (Kerguelen archipelago): a record
538 of glacier retreat, sedimentary mass wasting and southern Westerly intensification.
539 *Antarct. Sci.* 24, 608–618. <https://doi.org/10.1017/S0954102012000466>
- 540 Ikehara, K., 2015. Marine tephra in the Japan Sea sediments as a tool for paleoceanography
541 and paleoclimatology. *Prog. Earth Planet. Sci.* 2, 36. <https://doi.org/10.1186/s40645-015-0068-z>
- 542
- 543 McCormac, F.G., Hogg, A.G., Blackwell, P.G., Buck, C.E., Higham, T.F.G., Reimer, P.J.,
544 2004. Shcal04 Southern Hemisphere Calibration, 0–11.0 Cal Kyr BP. *Radiocarbon* 46,
545 1087–1092. <https://doi.org/10.1017/S0033822200033014>
- 546 Nesje, A., 1992. A Piston Corer for Lacustrine and Marine Sediments. *Arct. Alp. Res.* 24,
547 257. <https://doi.org/10.2307/1551667>
- 548 Oppedal, Bilt, W.G.M. van der, Balascio, N.L., Bakke, J., 2018. Patagonian ash on sub-
549 Antarctic South Georgia: expanding the tephrostratigraphy of southern South America
550 into the Atlantic sector of the Southern Ocean. *J. Quat. Sci.* 33, 482–486.
551 <https://doi.org/10.1002/jqs.3035>
- 552 Oppedal, L.T., Bakke, J., Paasche, Ø., Werner, J.P., van der Bilt, W.G.M., 2018. Cirque
553 Glacier on South Georgia Shows Centennial Variability over the Last 7000 Years.
554 *Front. Earth Sci.* 6, 2. <https://doi.org/10.3389/feart.2018.00002>

- 555 Peterse, F., Vonk, J.E., Holmes, R.M., Giosan, L., Zimov, N., Eglinton, T.I., 2014. Branched
556 glycerol dialkyl glycerol tetraethers in Arctic lake sediments: Sources and implications
557 for paleothermometry at high latitudes. *J. Geophys. Res. Biogeosciences* 119, 1738–
558 1754. <https://doi.org/10.1002/2014JG002639>
- 559 R Development Core Team, 2011. R: a Language and Environment for Statistical Computing.
560 R Foundation for Statistical Computing, Vienna.
- 561 Reyss, J.-L., Schmidt, S., Legeleux, F., Bonte, P., 1995. Large low background well type
562 detectors for measurements of environmental radioactivity. *Nucl Instrum Methods*
563 357, 391–397.
- 564 Ribeiro Guevara, S., Meili, M., Rizzo, A., Daga, R., Arribère, M., 2010. Sediment records of
565 highly variable mercury inputs to mountain lakes in Patagonia during the past
566 millennium. *Atmospheric Chem. Phys.* 10, 3443–3453. [https://doi.org/10.5194/acp-](https://doi.org/10.5194/acp-10-3443-2010)
567 10-3443-2010
- 568 Roche-Bellair, N., 1976. Les variations climatiques de l’holocène supérieur des îles
569 Kerguelen: d’après la coupe d’une tourbière de la plaine de Dante (côte méridionale).
570 *Comptes Rendus Académie Sci. Sér. D* 282, 1257–1260.
- 571 Saunders, K.M., Roberts, S.J., Perren, B., Butz, C., Sime, L., Davies, S., Van Nieuwenhuyze,
572 W., Grosjean, M., Hodgson, D.A., 2018. Holocene dynamics of the Southern
573 Hemisphere westerly winds and possible links to CO2 outgassing. *Nat. Geosci.*
574 <https://doi.org/10.1038/s41561-018-0186-5>
- 575 Shulmeister, J., Goodwin, I., Renwick, J., Harle, K., Armand, L., McGlone, M.S., Cook, E.,
576 Dodson, J., Hesse, P.P., Mayewski, P., Curran, M., 2004. The Southern Hemisphere
577 westerlies in the Australasian sector over the last glacial cycle: a synthesis. *Quat. Int.,*
578 *Climates, human, and natural system of the PEP2 transect* 118–119, 23–53.
579 [https://doi.org/10.1016/S1040-6182\(03\)00129-0](https://doi.org/10.1016/S1040-6182(03)00129-0)
- 580 Sijp, W.P., England, M.H., 2009. Southern Hemisphere Westerly Wind Control over the
581 Ocean’s Thermohaline Circulation. *J. Clim.* 22, 1277–1286.
582 <https://doi.org/10.1175/2008JCLI2310.1>
- 583 van Achterbergh, E., Griffin, W.L., Stiefenhofer, J., 2001. Metasomatism in mantle xenoliths
584 from the Letlhakane kimberlites: estimation of element fluxes. *Contrib. Mineral.*
585 *Petrol.* 141, 397–414. <https://doi.org/10.1007/s004100000236>
- 586 van der Bilt, W.G.M., Bakke, J., Werner, J.P., Paasche, Ø., Rosqvist, G., Vatile, S.S., 2017.
587 Late Holocene glacier reconstruction reveals retreat behind present limits and two-
588 stage Little Ice Age on subantarctic South Georgia. *J. Quat. Sci.* 32, 888–901.
589 <https://doi.org/10.1002/jqs.2937>
- 590 Van der Putten, N., Hébrard, J.-P., Verbruggen, C., Van de Vijver, B., Disnar, J.-R., Spassov,
591 S., de Beaulieu, J.-L., De Dapper, M., Keravis, D., Hus, J., Thouveny, N., Frenot, Y.,
592 2008. An integrated palaeoenvironmental investigation of a 6200 year old peat
593 sequence from Ile de la Possession, Iles Crozet, sub-Antarctica. *Palaeogeogr.*
594 *Palaeoclimatol. Palaeoecol.* 270, 179–195.
595 <https://doi.org/10.1016/j.palaeo.2008.09.014>
- 596 Van der Putten, N., Stieperaere, H., Verbruggen, C., Ochyra, R., 2004. Holocene
597 palaeoecology and climate history of South Georgia (sub-Antarctica) based
598 on a macrofossil record of bryophytes and seeds. *The Holocene* 14, 382–392.
599 <https://doi.org/10.1191/0959683604hl714rp>
- 600 Van der Putten, N., Verbruggen, C., Björck, S., Michel, E., Disnar, J.-R., Chapron, E., Moine,
601 B.N., de Beaulieu, J.-L., 2015. The Last Termination in the South Indian Ocean: A
602 unique terrestrial record from Kerguelen Islands (49°S) situated within the Southern
603 Hemisphere westerly belt. *Quat. Sci. Rev.* 122, 142–157.
604 <https://doi.org/10.1016/j.quascirev.2015.05.010>

605 Weis, D., Frey, F.A., Giret, A., Cantagrel, J.-M., 1998. Geochemical Characteristics of the
 606 Youngest Volcano (Mount Ross) in the Kerguelen Archipelago: Inferences for Magma
 607 Flux, Lithosphere Assimilation and Composition of the Kerguelen Plume. *J. Petrol.*
 608 39, 973–994. <https://doi.org/10.1093/etroj/39.5.973>
 609 Wessels, M., 1998. Natural environmental changes indicated by Late Glacial and Holocene
 610 sediments from Lake Constance, Germany. *Palaeogeogr. Palaeoclimatol. Palaeoecol.*
 611 140, 421–432. [https://doi.org/10.1016/S0031-0182\(98\)00026-1](https://doi.org/10.1016/S0031-0182(98)00026-1)
 612
 613
 614
 615
 616



617 S1. Scheme of different core sections taken in Lake Armor site 14-I (perched basin) and 14-II (deep
 618 basin) during the 2014 PALAS expedition. Background colours reflect the number of sections
 619 available for a given depth, from 4 (X4) to 1 (X1). NB: those depths correspond to measurements
 620 makes on the field, due to further decompression of the sediment, they are slightly different from
 621 model-depths used while referring sample depths in the paper. Results from section ARM14-II 03 C
 622 were not presented in this paper.
 623
 624
 625



626
627
628
629
630

Figure S2 : From left to right : $^{210}\text{Pb}_{\text{ex}}$ activities, ^{137}Cs and ^{241}Am activities, and the age model for the upper 10 cm of ARM14 II computed thanks to *serac* R package (Bruehl and Sabatier, 2020).